Eidgenössische Technische Hochschule Zürich
Swiss Federal Institute of Technology Zurich

Fourth-order non-linearity in a hybrid between superconducting qubit and high overtone bulk acoustic wave resonator

Semester thesis

Fernanda Banic Viana Martins
fmartins@student.ethz.ch

Laboratory for Solid State Physics
Departement of Physics, D-PHYS
ETH Zürich

Supervisors:
Prof. Yiwen Chu
Uwe von Lüpke

July 21, 2020

Abstract

This project explores the effects of a fourth-order non-linearity in a driven multimode quantum system on the example of a hybrid between a superconducting qubit and a high overtone bulk acoustic wave resonator. Using the quantum package QuTiP, we simulate the time evolution of the phonons under conditions that implement different operations of experimental relevance: the phonon drive, the SWAP gate and the CZ gate. Our results indicate that it is viable to implement quantum operations described by quartic terms in our system; however, further investigation is needed to fully describe them considering possible competing effects.

Contents

Chapter 1

Introduction

Much of the latest progress toward quantum information networks was accomplished by coupling superconducting qubits to acoustic resonators, which allowed for the investigation of quantum states of mechanical motion [1]. In this project, we employ the python package QuTiP to investigate quantum effects that are experimentally achievable considering a circuit quantum acoustodynamics (cQAD) system and its fourth-order nonlinearity, which allows for the manipulation of the interactions between the qubit and the phonon modes. This chapter summarizes the background information needed to understand the integration between qubits and phononic systems. First, we briefly introduce the theory behind transmon superconducting qubits in Section 1.1. Then, we discuss the utility of exploring quantum phenomena in the framework of mechanics, instead of electromagnetic waves, and present current implementations of such systems in Section 1.2. Finally, in Section 1.3, we present a potential application of cQAD systems in the storage of quantum information proposed by Hann et al. [2]. This proposal and its prospects are the starting point for this project.

1.1. Superconducting qubits

A Josephson junction is a non-linear inductor described by the Cooper-pair box Hamiltonian

$$H_{\mathrm{CPB}} = 4E_C(\hat{n} - n_g)^2 - E_J \cos(\hat{\phi}), \tag{1.1}$$

where E_C and E_J are the charging and the Josephson energy, respectively, ϕ is the flux across the junction, $\hat{n}$ is the Cooper-pair number operator conjugate to $\hat{\phi}$ ($[\hat{n}, \hat{\phi}] = i$) and n_g is the offset charge caused by the electrostatic environment [3].

The transmon regime of the Josephson junction provides one important case of a strongly non-linear harmonic oscillator: the transmon superconducting qubit. In this regime $E_J \gg E_C$ and the anharmonicity becomes dominant over the fluctuations of n_g [4]. Then, the Hamiltonian of transmon qubit is given by

$$H_q = 4E_C\ \hat{n}^2 - E_J \cos(\hat{\phi}). \tag{1.2}$$

The flux ϕ is small in the transmon limit, which allows us to expand the $\cos(\phi)$ term

in Eq. 1.2 as a harmonic potential with higher order corrections [5]:

$$\begin{aligned} H_q &= 4E_c\ \hat{n}^2 + \frac{1}{2}E_J\hat{\phi}^2 - \frac{1}{4!}E_J\hat{\phi}^4 + \mathcal{O}(\phi^6) \\ &\approx \hbar\omega\hat{q}^\dagger\hat{q} - \frac{1}{4!}E_J\phi_0^4(\hat{q}^\dagger + \hat{q})^4, \end{aligned} \tag{1.3}$$

where q corresponds to the annihilation operator of the qubit, $\hat{\phi} = \phi_0(q + q^\dagger)$ and $\phi_0 \propto (2E_C/E_J)^{1/4}$. Note that the second term contains 4^{th} order terms in $\hat{q}$ and $\hat{q}^\dagger$. Keeping only the energy conserving terms, the transmon qubit Hamiltonian becomes

$$H_q = \hbar\omega\hat{q}^\dagger\hat{q} - \frac{\alpha}{2}\hat{q}^\dagger\hat{q}^\dagger\hat{q}\hat{q}, \tag{1.4}$$

where $\alpha = E_J/2\phi_0^4$ is the anharmonicity. This anharmonicity in the transmon regime allows for the qubit to be operated as an effective two-level system [3].

1.2. Phonons for quantum mechanics

In order to perform quantum information tasks with transmon qubits, it is necessary to gain fine control over the interaction of the qubit with other elements in its environment [4]. In circuit quantum electrodynamics (cQED), for example, interactions between qubits are engineered by coupling the transmon Josephson junctions to a microwave environment with discrete photon modes [4, 6].

Similar to cQED, circuit quantum acoustodynamics (cQAD) employs superconducting transmon qubits to control mechanical—instead of electromagnetic—degrees of freedom by using phononic—instead of photonic—cavity modes [1, 7]. At similar frequencies of operation, acoustic resonators are more compact than their electromagnetic counterparts because the speed of sound is much lower than that of light [1, 8]. As a consequence, mechanical resonators provide more modes that can be individually explored with qubits [1]. Acoustic modes can also be isolated very well from their environments and achieve high quality factors ranging from $\sim 10^5$ to 10^{10} depending on the device type [9–11].

Several experimental setups have achieved control over mechanical degrees of freedom by coupling qubits to flexural modes in suspended beams [12], surface acoustic wave (SAW) resonators [13–16], and bulk acoustic wave (BAW) resonators [17–21]. The high-overtone bulk acoustic resonator (HBAR), a type of BAW resonator, has shown to be a particularly effective and promising low-loss phonon source [7, 19, 20].

Recently, Chu and co-workers have developed the $\hbar$BAR device, a combination of an HBAR and a superconducting qubit, and demonstrated that cQAD systems can be used to prepare, control and characterize quantum states of motion in a macroscale mechanical resonator [1]. This cQAD system, which can be a powerful component in quantum circuits, is an important example of the usefulness of Josephson junctions, whose non-linearity is exploited to achieve non-classical states of motion.

1.3. Applications in quantum computing

Considering the promising capabilities of devices such as BAW and SAW resonators, a scalable and hardware-efficient quantum random access memory (QRAM) implementation for multimode cQAD systems has been proposed recently [2]. In multimode cQAD, a transmon is piezoelectrically coupled to many phononic modes simultaneously, which can be accomplished in a high-Q, single chip device such as an HBAR [19]. In the proposed architecture, quantum information is stored in high-quality acoustic modes and interactions between phonon modes are manipulated via the application of off-resonant drives to the transmon qubit.

This architecture relies on the virtual excitation of an ancillary superconducting transmon qubit to mitigate the qubit decoherence, which occurs in a much shorter timescale when compared to that of the phonons. The qubit acts as a four-wave mixer [22–24] due to its 4^{th} order non-linearity, described in Section 1.1. As a result, phonons can be converted from one frequency to another by driving the transmon.

In this work, we simulate this system considering the multimode cQAD Hamiltonian, which will be presented in Chapter 2. Chapter 3 reports on the interaction between a qubit and a single phonon mode and between a qubit and three phonon modes, engineered by up to two drives. For the first system, we estimate how strong of a drive can be applied and how large of a coherent state can be obtained. For the second, we investigate different resonant effects—which stem from the Kerr non-linearity—that can be used to drive the phonon on resonance and to achieve the CZ and the SWAP gate. In Chapter 4 we summarize the outcomes of this work and present potential future directions and points of improvement.

Chapter 2

Theory

2.1. Multimode cQAD

In multimode cQAD, a transmon is piezoelectrically coupled to several acoustic modes. The Hamiltonian describing this system is given by

$$H = \omega_q q^\dagger q - \frac{\alpha}{2} q^\dagger q^\dagger q q + \sum_k (\omega_k m_k^\dagger m_k + g_k q^\dagger m_k + g_k^* q m_k^\dagger) + H_d, \tag{2.1}$$

where we treat the transmon as an anharmonic oscillator with Kerr non-linearity α coupled with strength g_k to the k^{th} phonon mode, q and m_k are the annihilation operators for the transmon and phonon modes, respectively, and

$$H_d = \sum_j \Omega_j q^\dagger e^{-i\omega_j t} + \text{H.c.} \tag{2.2}$$

describes the j^{th} external drive of strength Ω_j.

The application of off-resonant drives to the transmon can be used to harness interactions between phonon modes. As mentioned in Section 1.2, the transmon can act as a four-wave mixer due to its Kerr nonlinearity. As a result, driving the transmon at different frequencies can convert phonons from one frequency to another [2].

In order to write down this Hamiltonian in a form which exhibits terms that describe specific interactions between the phonon modes, a series of unitary operations must be performed. The derivation, taken from Ref. [2], starts with Eq. 2.1 and the operation

$$U_1 = e^{iH_0 t}, \tag{2.3}$$

where $H_0 = \omega_q q^\dagger q + \sum_k \omega_k m_k^\dagger m_k$.

The Hamiltonian becomes:

$$H = -\frac{\alpha}{2} q^\dagger q^\dagger q q + \sum_k (g_k m_k q^\dagger e^{-i\delta_k t} + \text{H.c.}) + \sum_j (\Omega_j q^\dagger e^{-i\delta_j t} + \text{H.c.}), \tag{2.4}$$

where $\delta_k = \omega_k - \omega_q$ and $\delta_j = \omega_j - \omega_q$ are, respectively, the detuning of the k^{th} phonon mode and of the j^{th} drive tone with respect to the qubit frequency. For ease of notation,

we introduce dimensionless parameters to describe the coupling strength of the phonon,

$$\lambda_k \equiv g_k/\delta_k, \tag{2.5}$$

and the strength of the drive,

$$\xi_j \equiv \Omega_j/\delta_j, \tag{2.6}$$

with respect to their detunings.

Then, we perform two additional transformations:

$$U_2 = \exp\Big(\sum_k (\lambda_k^* m_k^\dagger q e^{i\delta_k t} - \text{H.c.})\Big) \tag{2.7}$$

eliminates the qubit-phonon couplings to leading order in λ_k, and

$$U_3 = \exp\Big(\sum_j (\xi_j^* q e^{i\delta_j t} - \text{H.c.})\Big) \tag{2.8}$$

eliminates the drives. Together, these unitary transformations allow for the mapping

$$q \to q + \sum_j \xi_j e^{-i\delta_j t} + \sum_k \lambda_k m_k e^{-i\delta_k t} \equiv Q, \tag{2.9}$$

and the Hamiltonian becomes:

$$H = -\frac{\alpha}{2} Q^\dagger Q^\dagger Q Q, \tag{2.10}$$

where linear terms of the form $\Omega_j^* \lambda_k m_k e^{i(\delta_j - \delta_k)t} +$ H.c. are omitted, which is justified in the rotating-wave approximation if the drives are far detuned from the phonon modes ($|\delta_j - \delta_k| \gg \Omega_j \lambda_k$).

2.2. Expansion

We can now obtain a cQAD Hamiltonian with terms that clearly describe particular interactions between the phonon modes by expanding Eq. 2.10 into several summations. Because $Q = q + \sum_j \xi_j e^{-i\delta_j t} + \sum_k \lambda_k m_k e^{-i\delta_k t}$, each term must have four *components*, which are either a qubit operator, a phonon operator accompanied by a factor of λ or a drive ξ. The final expression contains terms with four ($q^\dagger q^\dagger q q$), three ($q^\dagger q^\dagger q$), two ($q^\dagger q^\dagger$ or $q^\dagger q$), one ($q^\dagger$) and zero qubit operators, along with all combinations of the remaining components—such that the total of four components per term is preserved. This gives rise to $6^4 = 1296$ terms, which can be summarized in twenty-one convenient summations, each with a particular pre-factor, and their respective Hermitian conjugate.

$$
\begin{aligned}
H = -\frac{\alpha}{2}\Bigg(&\frac{1}{2}q^\dagger q^\dagger qq + 2\sum_j \xi_j q^\dagger q^\dagger q e^{-i\delta_j t} + 2\sum_k \lambda_k m_k q^\dagger q^\dagger q e^{-i\delta_k t} \\
&+ 2\sum_{ij} \xi_i^* \xi_j q^\dagger q e^{i(\delta_i-\delta_j)t} + 4\sum_{jk} \xi_j^* \lambda_k m_k q^\dagger q e^{i(\delta_j-\delta_k)t} \\
&+ 2\sum_{kl} \lambda_k^* \lambda_l m_k^\dagger m_l q^\dagger q e^{i(\delta_k-\delta_l)t} + \sum_{ij} \xi_i \xi_j q^\dagger q^\dagger e^{-i(\delta_i+\delta_j)t} \\
&+ \sum_{kl} \lambda_k \lambda_l m_k m_l q^\dagger q^\dagger e^{-i(\delta_k+\delta_l)t} + 2\sum_{jk} \xi_j \lambda_k m_k q^\dagger q^\dagger e^{-i(\delta_j+\delta_k)t} \\
&+ 2\sum_{hij} \xi_h^* \xi_i \xi_j q^\dagger e^{i(\delta_h-\delta_i-\delta_j)t} + 2\sum_{jkl} \xi_j^* \lambda_k \lambda_l m_k m_l q^\dagger e^{i(\delta_j-\delta_k-\delta_l)t} \\
&+ 4\sum_{ijk} \xi_i^* \xi_j \lambda_k m_k q^\dagger e^{i(\delta_i-\delta_j-\delta_k)t} + 4\sum_{kjl} \xi_j \lambda_k^* \lambda_l m_k^\dagger m_l q^\dagger e^{i(\delta_k-\delta_j-\delta_l)t} \\
&+ 2\sum_{kij} \xi_i \xi_j \lambda_k^* m_k^\dagger q^\dagger e^{i(\delta_k-\delta_i-\delta_j)t} + 2\sum_{klm} \lambda_k^* \lambda_l \lambda_m m_k^\dagger m_l m_m q^\dagger e^{i(\delta_k-\delta_l-\delta_m)t} \\
&+ \frac{1}{2}\sum_{ghij} \xi_g^* \xi_h^* \xi_i \xi_j e^{i(\delta_g+\delta_h-\delta_i-\delta_j)t} + \frac{1}{2}\sum_{klmn} \lambda_k^* \lambda_l^* \lambda_m \lambda_n m_k^\dagger m_l^\dagger m_m m_n e^{i(\delta_k+\delta_l-\delta_m-\delta_n)t} \\
&+ \sum_{ijkl} \xi_i^* \xi_j^* \lambda_k \lambda_l m_k m_l e^{i(\delta_i+\delta_j-\delta_k-\delta_l)t} + \underbrace{2\sum_{hijk} \xi_h^* \xi_i^* \xi_j \lambda_k m_k e^{i(\delta_h+\delta_i-\delta_j-\delta_k)t}}_{\text{XIX: Phonon drive}} \\
&+ \underbrace{2\sum_{kljm} \xi_j \lambda_k^* \lambda_l^* \lambda_m m_k^\dagger m_l^\dagger m_m e^{i(\delta_k+\delta_l-\delta_j-\delta_m)t}}_{\text{XX: CZ}} \\
&+ \underbrace{2\sum_{ikjl} \xi_i^* \xi_j \lambda_k^* \lambda_l m_k^\dagger m_l e^{i(\delta_i+\delta_k-\delta_j-\delta_l)t}}_{\text{XXI: SWAP}} + \text{H.c.}\Bigg)
\end{aligned}
\tag{2.11}
$$

In the cQAD system that we will simulate in Chapter 3, there are three phonon modes and up to two drive tones. Then, the phonon-mode indices k, l, m and n in Eq. 2.11 range from one to three, while g, h, i and j, the drive indices, range from one to two. The summations give rise to a total of 1296 terms in the Hamiltonian.

2.3. Considerations on individual resonant terms

A term in the Hamiltonian expansion (Eq. 2.11) implements a particular operation when its resonance condition is met, i.e., when the detunings of the laser drives and phonons are such that the exponent of the term becomes zero. We can thus turn on a specific effect in our system by choosing the appropriate detunings. In Chapter 3, we will focus on the terms which implement the phonon drive (XIX), the controlled-Z, or CZ, gate (XX), and the SWAP gate (XXI).

The effect of each term is expected to take place with an evolution time of $t = \pi/g_\nu$, where the virtual coupling rate g_ν is determined by the pre-factor of the term, accounting also for its Hermitian conjugate. For example, the exchange of the states of phonon modes A and B occurs with the evolution under the SWAP gate term for a time $t = \pi/(2\alpha\xi_1^*\xi_2\lambda_A^*\lambda_B)$. We note that evolution under this same term (XXI) for half of that time results in a 50:50 beam splitter operation [2, 23].

Additionally, term XXI also represents a Stark shift of the phonon modes. In order to account for this effect when considering evolution under the full Hamiltonian (Eq. 2.1), we calculate the Stark-shifted detuning of the k^{th} phonon mode due to the j^{th} drive

$$\tilde{\delta_k} = \delta_k - 2\alpha\lambda_k^2 \sum_j |\xi_j|^2 \tag{2.12}$$

and use it to meet the resonant condition of each term of interest.

In the course of this project, python scripts were developed to efficiently compute the summations in each term of Eq. 2.11. The implemented strategy differs from the typical approach of using the *args* variable to solve problems with time-dependent Hamiltonians in QuTiP [25]. A sample script can be found in Appendix A.

Chapter 3

Simulations

This chapter reports on the results of simulating a cQAD system composed by one qubit, three phonon modes and up to two drive tones. For each of the four quantum objects—the transmon and the three phonons—we implement a simulation considering a two-level Hilbert space. Using the python package QuTiP, we solve the master equation for the cQAD Hamiltonian from Eq. 2.1 in the frame rotating with the qubit frequency:

$$H = -\frac{\alpha}{2} q^\dagger q^\dagger q q + \sum_k \left(\delta_k m_k^\dagger m_k + g_k m_k^\dagger q + \ g_k^* m_k q^\dagger \right) + \sum_j \left(\Omega_j q^\dagger e^{-i\delta_j t} + \ \text{H.c.} \right). \quad (3.1)$$

We aim to simulate the conditions of a device in which a transmon qubit is piezoelectrically coupled to two high-overtone bulk acoustic resonators. In Chapter 2, we have identified the terms of interest and their resonant conditions. Here, we simulate the evolution of the system under the Hamiltonian in Eq. 3.1 with the goal to determine whether the effects would be observable in experimental conditions.

To implement the phonon drive, we consider lifetimes of $T_1 = 7$ µs for the qubit and of $T_1 = 100$ µs and $T_2 = 40$ µs for the phonons, which were previously achieved in an $\hbar$BAR device [1]. We use a slightly larger T_2 of 60 µs for the CZ gate and the SWAP gate. For each implementation, we will discuss the parameters—such as the drive strength, the coupling strength and the detunings—which enable the target operation, as well the limitations associated with using single quartic terms (Eq. 2.11) to make predictions about the evolution of our system. The obtained values can serve as guidelines in future experimental realizations of quantum operations in an $\hbar$BAR device.

3.1. Phonon drive

In the expanded Hamiltonian (Eq. 2.11), the phonon drive corresponds to term XIX:

$$-\frac{\alpha}{2} \sum_{hijl} \xi_h^* \xi_i^* \xi_j \lambda_k m_k e^{i(\delta_h + \delta_i - \delta_j - \delta_k)t} + \text{H.c.} \quad (3.2)$$

This term allows for the excitation of a phonon mode via the application of one resonant frequency.

3.1.1. Phonon-qubit interaction

First, we will consider the interaction between a qubit and a single phonon to find an upper bound for the drive strength ξ_1 that should be used experimentally. Because the lifetime of our qubits is much less than that of phonons in our HBAR resonator, exciting the qubit severely limits the timescale of quantum gates and operations in our system. In general, the drive strength determines the pulse duration that is required for the effects of selected phonon excitations to take place. Thus, we aim to find an optimal value that excites the phonons in the desired timescale, while not indirectly exciting the ground-state qubit through the coupling of the transmon and phonon modes.

By simulating the interaction between a qubit and a single phonon, it is computationally viable to account for the large Hilbert space of the phonons and thus describe the system more realistically. To improve the computational speed we neglect the dephasing lifetime $T_2 = 40$ µs of the phonons, which plays no major role in the timescale relevant for the simulations in this section (< 15 µs).

We use the Hamiltonian from Eq. 3.1 containing a single phonon A and a single drive instead of a sum:

$$H = -\frac{\alpha}{2} q^\dagger q^\dagger q q + \delta_A m_A^\dagger m_A + g(m_A^\dagger q + q^\dagger m_A) + \Omega_1 q^\dagger e^{-i\delta_1 t} + \Omega_1 q e^{i\delta_1 t}. \tag{3.3}$$

Fig. 3.1 displays the average qubit and phonon populations during the application of drives of different magnitudes for a coupling strength of $g/2\pi = 0.5$ MHz. Partial excitation of the qubit occurs for all drive strengths, and an average population of $\langle n_q \rangle = 0.25$ is reached at $\xi_1 = 0.35$. Therefore, we estimate that $\xi_1 = 0.35$ should be used as a benchmark upper-limit for initial experimental investigations and for the simulations of the full system in the following sections. Note that in the transformations performed in the cQAD Hamiltonian (see Section 2.1) one of the assumptions was that $\xi_1 \ll 1$, so in order for the derived equations to be valid in our system, it is not advisable to employ dimensionless drive strengths close to 1.

We note that the size of the Hilbert space that was considered for the phonon ($N = 30$) is not sufficient to describe this interaction for pulse lengths greater than approximately 5 µs. This is a short timescale when compared to the lifetime of our qubit (7 µs), which limits the predictive power of these simulations. Employing larger Hilbert spaces leads to undesirably long computation times.

The simulation of the phonon-qubit interaction also allows us to estimate how large of a coherent state can be achieved in our system. We use QuTiP to plot the Wigner function of the resulting state after evolution under the Hamiltonian from Eq. 3.3 in the rotating frame of phonon A:

$$H = -\frac{\alpha}{2} q^\dagger q^\dagger q q + g m_A q^\dagger e^{-i\delta_A t} + g m_A^\dagger q e^{i\delta_A t} + \Omega_1 q^\dagger e^{-i\delta_1 t} + \Omega_1 q e^{i\delta_1 t}. \tag{3.4}$$

The Hamiltonian in Eq. 3.4 yields a computationally more efficient calculation and allows us to use a larger Hilbert space of $N = 50$ for the phonon. Fig. 3.2 indicates that a coherent state of $\alpha \approx 5$ is achieved after evolution for 12.3 µs using typical experimental

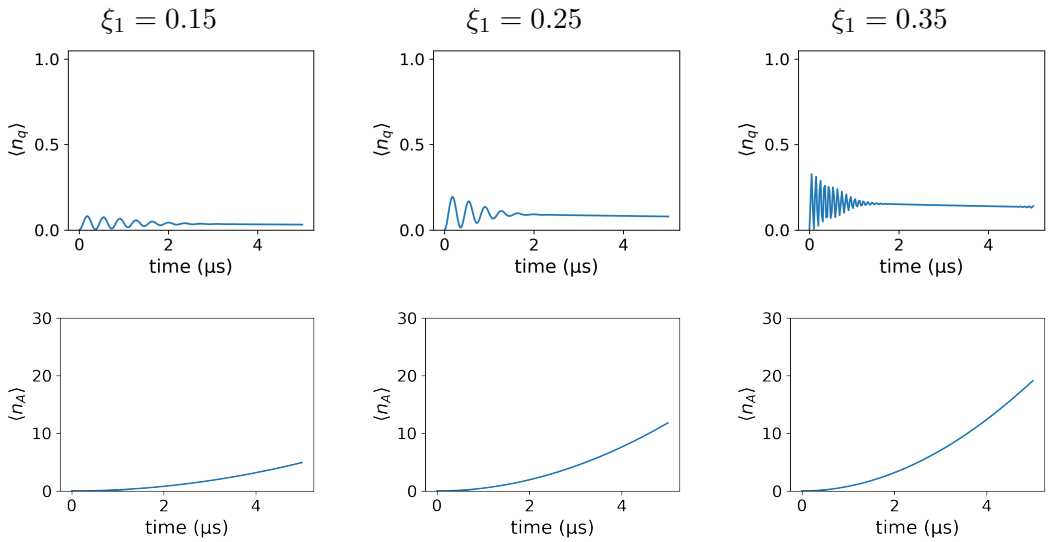

Figure 3.1.: Average populations of the qubit (top row) and of phonon mode A (bottom row) for $g/2\pi = 0.5$ MHz and selected values of the dimensionless drive strength ξ_1.

parameters. Given these preliminary results of the phonon drive, we now turn to studying this operation considering a multimode cQAD system.

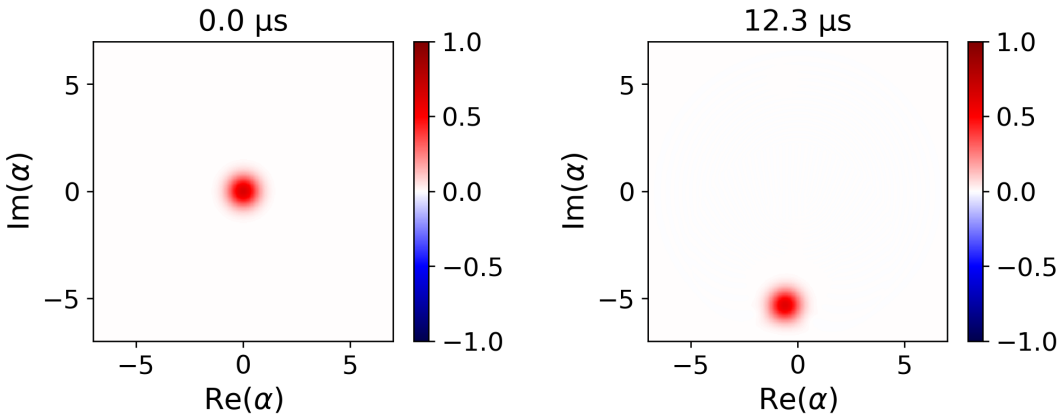

Figure 3.2.: Wigner functions of the states achieved at the resonance condition of the phonon drive ($\tilde{\delta}_1 = \tilde{\delta}_A$). A coherent state of $\alpha \approx 5$ ($\langle n \rangle \approx 25$) is achieved after evolution for 12.3 μs. The parameters are $\xi_1 = 0.15$, $g/2\pi = 0.5$ MHz, $\alpha/2\pi = 150$ MHz and $\delta_A/2\pi = 74$ MHz.

3.1.2. Phonon drive resonance condition in the cQAD Hamiltonian

In order to simulate the interaction between one qubit and three phonon modes, we model each of these objects as a two-level system. This reduction of the Hilbert space, when compared to that used in Section 3.1.1, can give rise to unphysical results. This can be seen in Fig. 3.3, which displays the time evolution of each quantum object of our system in the z-axis of the Bloch sphere according to the full cQAD Hamiltonian. We have enacted the phonon drive by initializing all the qubit and phonon modes in the ground state ($\psi_0 = |0,0,0,0\rangle$) and setting the detuning of the drive with respect to the qubit equal to the that of one of the phonon modes, in the example of phonon A ($\tilde{\delta}_1 = \tilde{\delta}_A$, considering the Stark-shifted frequencies). As expected, the qubit and phonons B and C remain in the ground. Phonon A, however, undergoes Rabi oscillations, which is a direct consequence of using a Hilbert space of size two, and not a physical phenomenon. The expected behavior under the phonon drive resonance condition with a larger Hilbert space, but considering only one phonon-qubit interaction, can be found in the previous section.

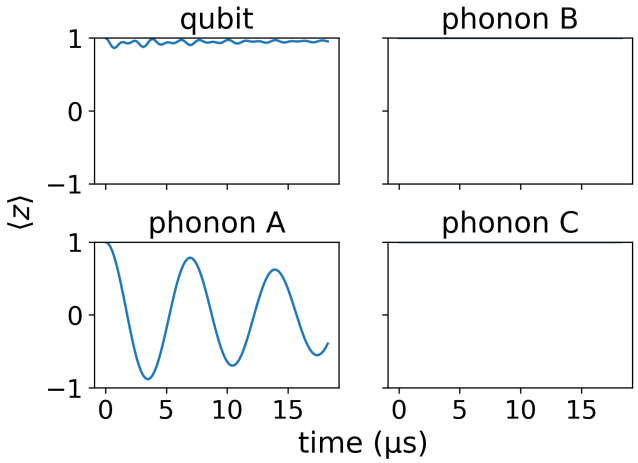

Figure 3.3.: Populations of the qubit and the phonon modes against time at the resonance condition of the phonon drive ($\tilde{\delta}_1 = \tilde{\delta}_A$, accounting for the Stark shift). Rabi oscillations are driven in phonon A, as characterized by oscillations in the expectation value of the z-axis of the Bloch sphere. The system is initialized in the ground state, $\psi_0 = |0,0,0,0\rangle$, and the parameters are $\xi_1 = 0.15$, $g/2\pi = 0.5$ MHz, $\alpha/2\pi = 150$ MHz, $\delta_A/2\pi = 74$ MHz, $\delta_B/2\pi = 114$ MHz, $\delta_C/2\pi = 54$ MHz.

Although they may give rise to unphysical Rabi oscillations, simulations using a Hilbert space with size $N = 2$ are very useful, as they allow us to account for the interaction between all the components of the full system. Further, the Rabi oscillations signal that the resonance condition of a given term from Eq. 2.11 was met. Fig. 3.4 displays the Rabi oscillations in phonon A as the detuning of the drive δ_1 is varied near the resonance

condition. The Rabi oscillations achieve the largest amplitude when $\tilde{\delta}_1 = \tilde{\delta}_A$, indicating that they are indeed a consequence of the phonon drive term.

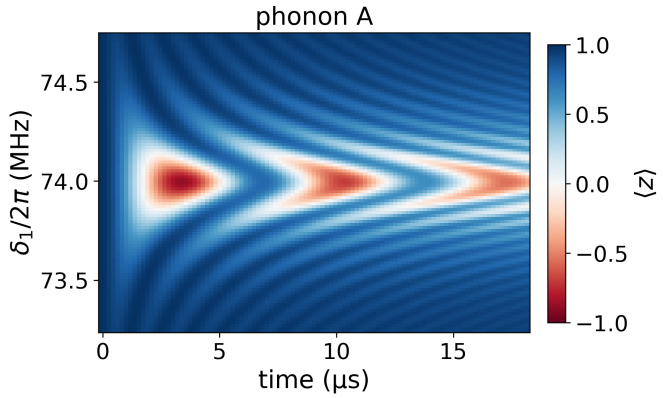

Figure 3.4.: Population of phonon A against time and drive detuning δ_1. When the resonance condition of the phonon drive ($\tilde{\delta}_1 = \tilde{\delta}_A$) is achieved, we observe the strongest Rabi oscillations. The color scale represents the expectation value of the z-axis of the Bloch sphere, in which -1 (red) corresponds to the excited state and $+1$ (blue) to the ground state. The system is initialized in the ground state, $\psi_0 = |0,0,0,0\rangle$, and the parameters are $\xi_1 = 0.15$, $g/2\pi = 0.5$ MHz, $\alpha/2\pi = 150$ MHz, $\delta_A/2\pi = 74$ MHz, $\delta_B/2\pi = 114$ MHz, $\delta_C/2\pi = 54$ MHz.

We note that the resonant effect of exciting one phonon mode occurs within a few microseconds. Considering the latest achieved lifetimes of phonons and qubits [1], this short timescale makes the phonon drive an effect of particular interest. The phonon drive could, for instance, be a component of algorithms involving other qubit gates, and it is thus important to investigate how quickly this effect can take place.

To that end, Fig. 3.5 displays the Rabi oscillations achieved by phonon A when the resonant condition is met for controllable experimental parameters. Fig. 3.5a shows that the Rabi oscillations can be made significantly faster by increasing ξ_1. Fig. 3.5b shows that the phonon drive is independent of the system's Kerr non-linearity α, as expected. Here, we considered a conservative estimate of $g/2\pi = 0.5$ MHz, but we note that if larger qubit-phonon coupling strengths are achieved in an experimental setting, the period of the Rabi oscillations can be further reduced.

3.1.3. Effects of the quartic term

Fig. 3.6a shows the time evolution of phonon A under the quartic term only (term XIX in Eq. 2.11), and not under the full Hamiltonian, as in the previous section. With all remaining conditions kept the same, we observe that the period and amplitude of the Rabi oscillations are greatly different.

The expected period of the phonon drive operation is π/g_ν, where the virtual coupling

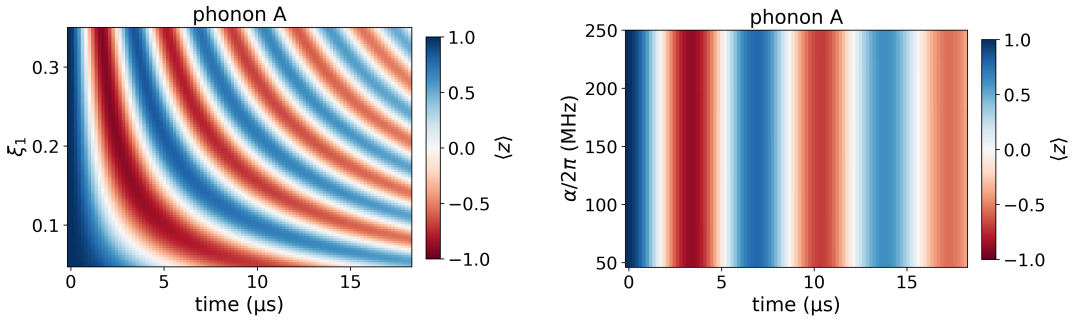

(a) (b)

Figure 3.5.: Population phonon A against time and (a) dimensionless drive strength ξ_1 and (b) Kerr non-linearity α at the resonance condition of the phonon drive, $\tilde{\delta}_1 = \tilde{\delta}_A$. Increasing ξ_1 results in significant faster Rabi oscillations, whereas large variations in α do not affect the phonon drive. The color scale and the parameters are the same as in Fig. 3.4.

rate $g_\nu = 2\alpha\xi_1^{*2}\xi_1\lambda_A$ is determined by the term's prefactors in Eq. 2.11 [2]. This corresponds to the period of ~ 70 μs observed when considering the quartic term only (Fig. 3.6a). The oscillation happens much faster when the resonance condition is met in the full Hamiltonian (Fig. 3.6b). This discrepancy suggests the presence of competing resonant or near-resonant effects that emerge in the actual system.

We note that in the derivation of Eq. 2.10, we have neglected linear terms considering the rotating-wave approximation. Here, however, the drive tones are not far detuned from the modes of interest, and these previously-omitted lower-order terms could explain the discrepancies. They are:

$$\begin{aligned} H_{\text{linear}} = g \sum_{mj} \Bigg(& \left(1 - \frac{\lambda_m^2}{2}\right)^2 q^\dagger m_m e^{-i\delta_m t} - \left(1 - \frac{\lambda_m^2}{2}\right) q^\dagger q e^{-i\delta_m t} \\ & + \lambda_m \left(1 - \frac{\lambda_m^2}{2}\right) m_m^\dagger m_m e^{-i\delta_m t} - \lambda_m^2 m_m^\dagger q e^{-i\delta_m t} \\ & + \underbrace{\xi_j \left(1 - \frac{\lambda_m^2}{2}\right) e^{i(\omega_j - \omega_m)t} m_m}_{\text{v}} - \lambda_m^2 \xi_j e^{i(\omega_j - \omega_m)t} q + \text{H.c.} \Bigg) \end{aligned} \tag{3.5}$$

Fig. 3.6c indicates that the addition of term v from Eq. 3.5 accounts for the difference in timing and amplitude almost completely, and that the Rabi oscillations have a very similar profile to that of the full Hamiltonian. This result indicates that the effects of the fourth-order non-linearity might be significantly modified by other processes that occur in the system.

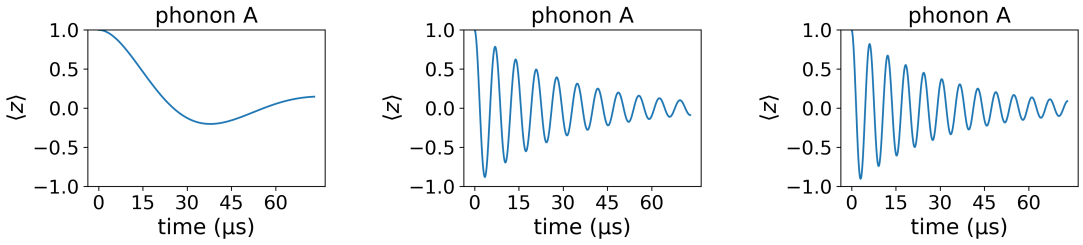

(a) (b) (c)

Figure 3.6.: Time evolution of the population of phonon A at the resonance condition of the phonon drive ($\tilde{\delta}_1 = \tilde{\delta}_A$) for one oscillation period, as determined by the effective coupling strength of the quartic term. The period of the Rabi oscillations considering the quartic term only (a) agrees with the predicted time and is much larger than that considering the full cQAD Hamiltonian (b). This timing difference is explained by a previously neglected linear term, which, when added to the quartic term, yields a near identical oscillation profile (c) when compared to (b). The parameters are $\xi_1 = 0.15$, $g/2\pi = 0.5$ MHz, $\alpha/2\pi = 150$ MHz, $\delta_A/2\pi = 74$ MHz, $\delta_B/2\pi = 114$ MHz, $\delta_C/2\pi = 54$ MHz.

3.2. CZ gate

We can engineer a three-mode interaction using a single drive tone with detuning $\delta_1 = \delta_A + \delta_B - \delta_C$ using term XX from Eq. 2.11:

$$-\alpha \sum_{kljm} \xi_j \lambda_k^* \lambda_l^* \lambda_m m_k^\dagger m_l^\dagger m_m e^{i(\delta_k+\delta_l-\delta_j-\delta_m)t} + \text{H.c.} \tag{3.6}$$

This interaction allows for the implementation of a controlled phase (CZ) gate, in which phonon C is initialized in the $|0\rangle$ state and acts as an ancilla, while phonons A and B are initialized in the excited state. Fig. 3.7 displays the effects of the CZ gate in the qubit and in the three phonons as we scan the detuning of the drive δ_1 across the resonance condition. The mapping $|0110\rangle_{\text{qABC}} \rightarrow |0001\rangle \rightarrow -|0110\rangle$ configures a CZ gate, as the system acquires a global geometric phase. This can be directly observed in Fig. 3.8, where the system is initialized in the $\psi_0 = |0, 1, (0+1)/\sqrt{2} \equiv +x, 0\rangle$ state. Then, the expectation value of the population in the x-axis of the the Bloch sphere changes sign during the time evolution, indicating the change in phase.

Fig. 3.9 displays the effects of the CZ operation in the qubit and phonon states while experimental parameters are scanned. Fig. 3.9 (top row) shows that, for the simulation conditions, the optimal ξ_1 is slightly below 0.20. Fig. 3.9 (middle row) shows that the phonon drive can be implemented for a wide range of α values, with an optimal near $\alpha/2\pi = 150$ MHz. Then, in Fig. 3.9 (bottom row), we scan the detuning of phonon B in a range that avoids a coincidental mode spacing, i.e., that ensures $|\delta_A - \delta_B| \neq |\delta_A - \delta_C|$.

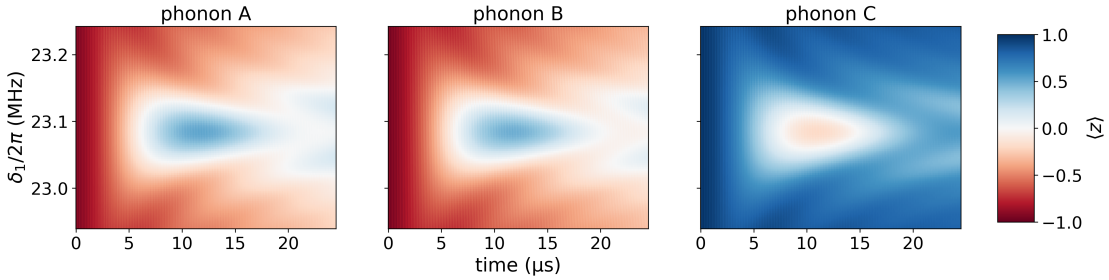

Figure 3.7.: Populations of the phonon modes A, B and C against time and drive detuning δ_1. When the resonance condition of the CZ gate ($\tilde{\delta}_1 = \tilde{\delta}_A + \tilde{\delta}_B - \tilde{\delta}_C$) is achieved, phonon C acts as ancilla. The color scale represents the expectation value of the z-axis of the Bloch sphere, in which -1 (red) corresponds to the excited state and +1 (blue) to the ground state. The system is initialized with phonons A and B in the excited state, $\psi_0 = |0, 1, 1, 0\rangle$, and the parameters are $\xi_1 = 0.19$, $g/2\pi = 2$ MHz, $\alpha/2\pi = 150$ MHz, $\delta_A/2\pi = 14$ MHz, $\delta_B/2\pi = 19$ MHz, $\delta_C/2\pi = 10$ MHz.

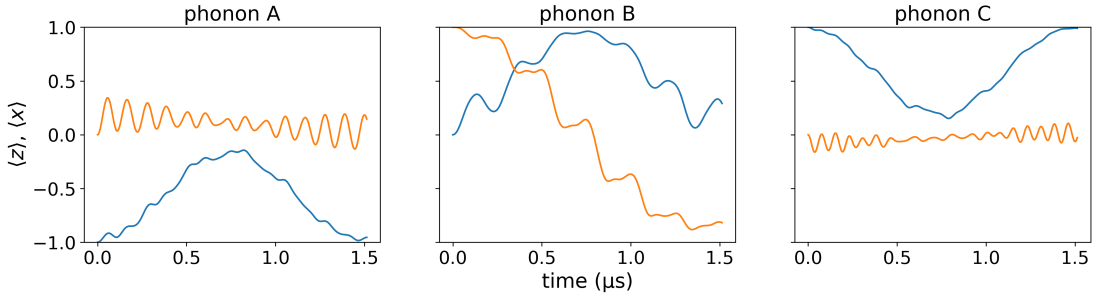

Figure 3.8.: Time evolution of the population of phonons A, B and C at the resonance condition of the CZ gate ($\tilde{\delta}_1 = \tilde{\delta}_A + \tilde{\delta}_B - \tilde{\delta}_C$). The blue (orange) line represents the expectation value of the population in the z-axis (x-axis) of the Bloch sphere. The change in $\langle x \rangle$ from 1 to -1 for phonon B indicates that the CZ gate indeed causes the system to acquire a global geometric phase. Here, the system is initialized in the $\psi_0 = |0, 1, (0 + 1)/\sqrt{2}, 0\rangle$ state and the parameters are $\xi_1 = 0.19$, $g/2\pi = 2$ MHz, $\alpha/2\pi = 150$ MHz, $\delta_A/2\pi = 14$ MHz, $\delta_B/2\pi = 19$ MHz, $\delta_C/2\pi = 10$ MHz.

The results indicate that the phonon drive is sensitive to the mode separation, and that, given the other simulation parameters, $\delta_B/2\pi \approx 19$ MHz is optimal.

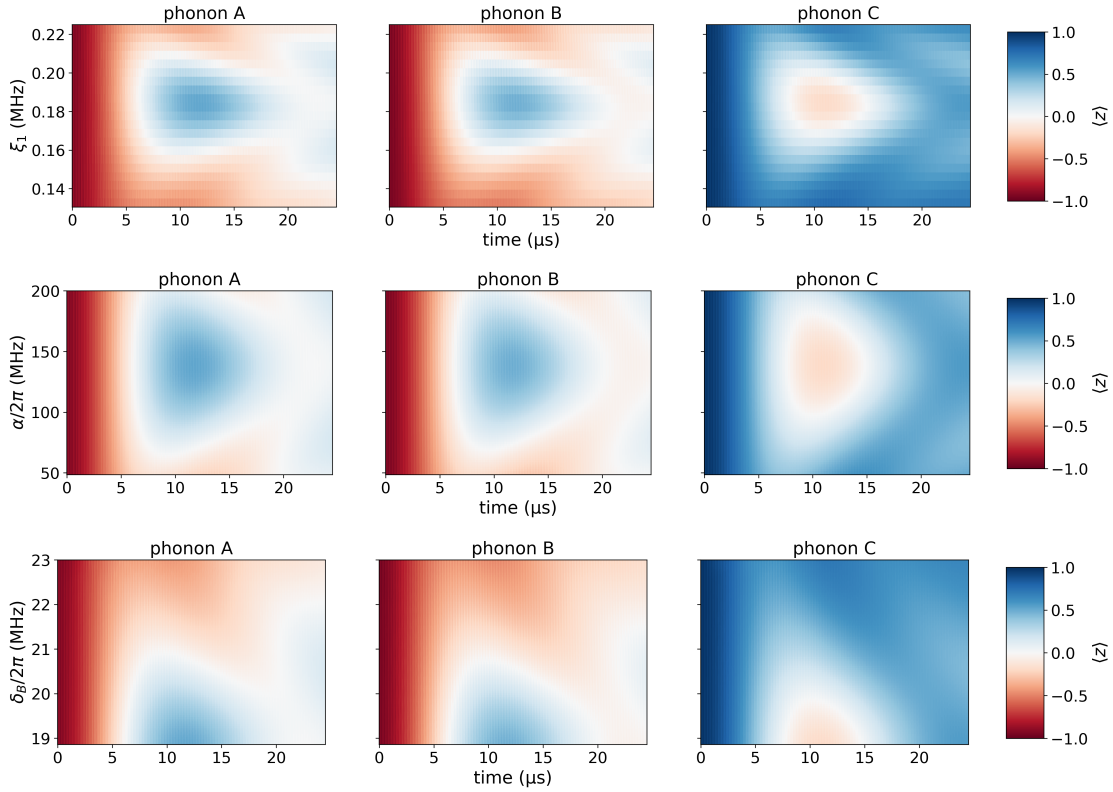

Figure 3.9.: Populations of phonon modes A, B and C against time and (top row) dimensionless drive strength ξ_1, (middle row) Kerr non-linearity α, and (bottom row) δ_B at the resonance condition of the CZ gate, $\tilde{\delta}_1 = \tilde{\delta}_A + \tilde{\delta}_B - \tilde{\delta}_C$. There is an optimal range for the three parameters. The color scale and other parameters are the same as in Fig. 3.7.

Fig. 3.10 indicates that the conditions that work for the full Hamiltonian also effect the CZ gate when using the quartic term individually. Unlike for the phonon drive, the addition of the linear terms identified in Eq. 3.5 does not explain the timing discrepancy that arises between these two implementations of the CZ operation. This indicates that there are other competing effects that change the timescale of our system, which could stem, for example, from coincidental resonances with other terms in the cQAD Hamiltonian (Eq. 2.11). We note that, in order to implement the CZ gate considering the full Hamiltonian, we had to assume a large coupling strength $g/2\pi = 2$ MHz and a small phonon-mode separation.

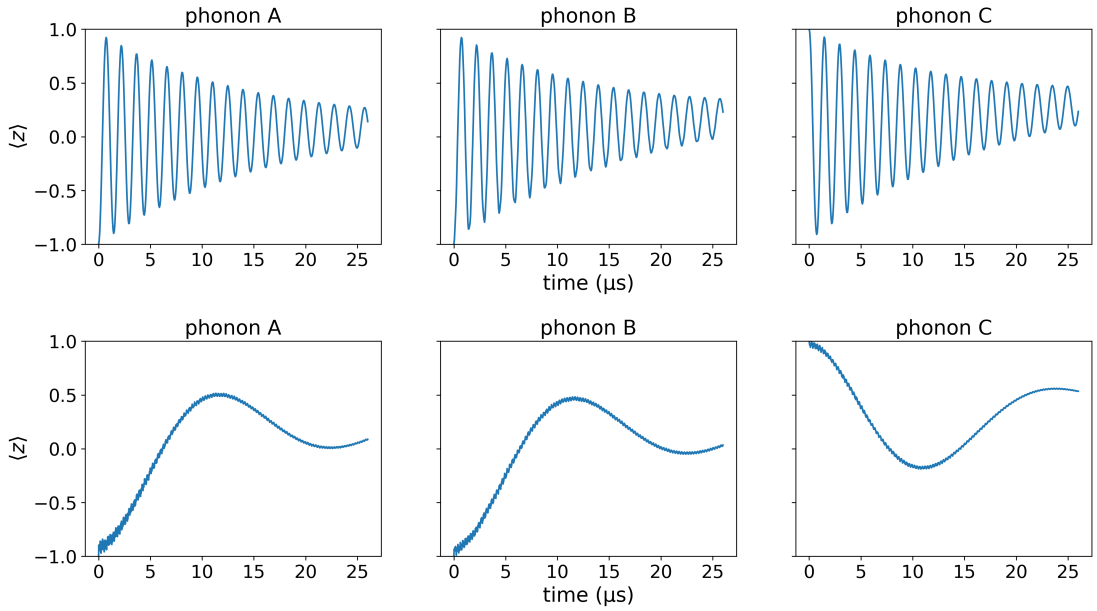

Figure 3.10.: Time evolution of the population of phonons A, B and C at the resonance condition of the CZ gate ($\tilde{\delta}_1 = \tilde{\delta}_A + \tilde{\delta}_B - \tilde{\delta}_C$). The period of the oscillations considering the CZ quartic term only (top row) is much shorter than when we consider the full cQAD Hamiltonian (bottom row). In both cases, the parameters are $\xi_1 = 0.19$, $g/2\pi = 2$ MHz, $\alpha/2\pi = 150$ MHz, $\delta_A/2\pi = 14$ MHz, $\delta_B/2\pi = 19$ MHz, $\delta_C/2\pi = 10$ MHz.

3.3. SWAP gate

We can implement the SWAP gate in our system through XXI from Eq. 2.11:

$$-\alpha \sum_{ikjl} \xi_i^* \xi_j \lambda_k^* \lambda_l m_k^\dagger m_l e^{i(\delta_i+\delta_k-\delta_j-\delta_l)t} + \text{H.c.}, \tag{3.7}$$

which effects a SWAP operation when we employ two drives whose frequency separation matches that between two phonon modes, for example, modes A and B ($\tilde{\delta}_1 = \tilde{\delta}_A - \tilde{\delta}_B + \tilde{\delta}_2$). In this manner, the excitation of a phonon in mode A of one resonator can be swapped into mode B of the other, for example. Fig. 3.11 displays the SWAP between phonons A and B as δ_1 is varied across the resonance condition.

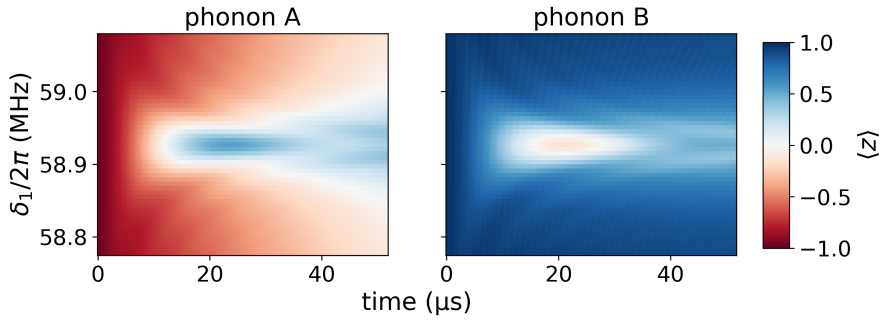

Figure 3.11.: Populations of phonon modes A and B against time and drive detuning δ_1. When the resonance condition of the SWAP gate ($\tilde{\delta}_1 = \tilde{\delta}_A - \tilde{\delta}_B + \tilde{\delta}_2$) is achieved, the excitation of phonons A and B swap. The color scale represents the expectation value of the z-axis of the Bloch sphere, in which -1 (red) corresponds to the excited state and +1 (blue) to the ground state. The system is initialized with phonon A in the excited state, $\psi_0 = |0, 1, 0, 0\rangle$, and the parameters are $\xi_1 = \xi_2 = 0.19$, $g/2\pi = 2.5$ MHz, $\alpha/2\pi = 150$ MHz, $\delta_A/2\pi = 44$ MHz, $\delta_B/2\pi = 64$ MHz, $\delta_C/2\pi = 26$ MHz, $\delta_2/2\pi = 79$ MHz.

Fig. 3.12 (top row) shows that the SWAP operation can be more quickly effected when the drive strengths ξ_1 and ξ_2 (which is scanned along with ξ_1) are slightly below 0.3, given the other parameters employed in the simulation. Fig. 3.12 (middle row) shows that this gate is more effective with a non-linearity of $\alpha/2\pi = 150$ MHz. Our simulation also indicates that a successful implementation of the SWAP gate is very restrictive in terms of mode separation, as can be seen in the bottom row of Fig. 3.12.

Similar to the CZ gate, achieving the SWAP operation with the simulation was only possible with a large coupling strength $g/2\pi = 2.5$ MHz, although the phonon-mode separation can be much larger than that in the previous section. Again, we were not able to identify a specific term that accounts for the differences between the time evolution under the full Hamiltonian and that under the SWAP quartic term (term XXI in Eq. 2.11), displayed in Fig. 3.13.

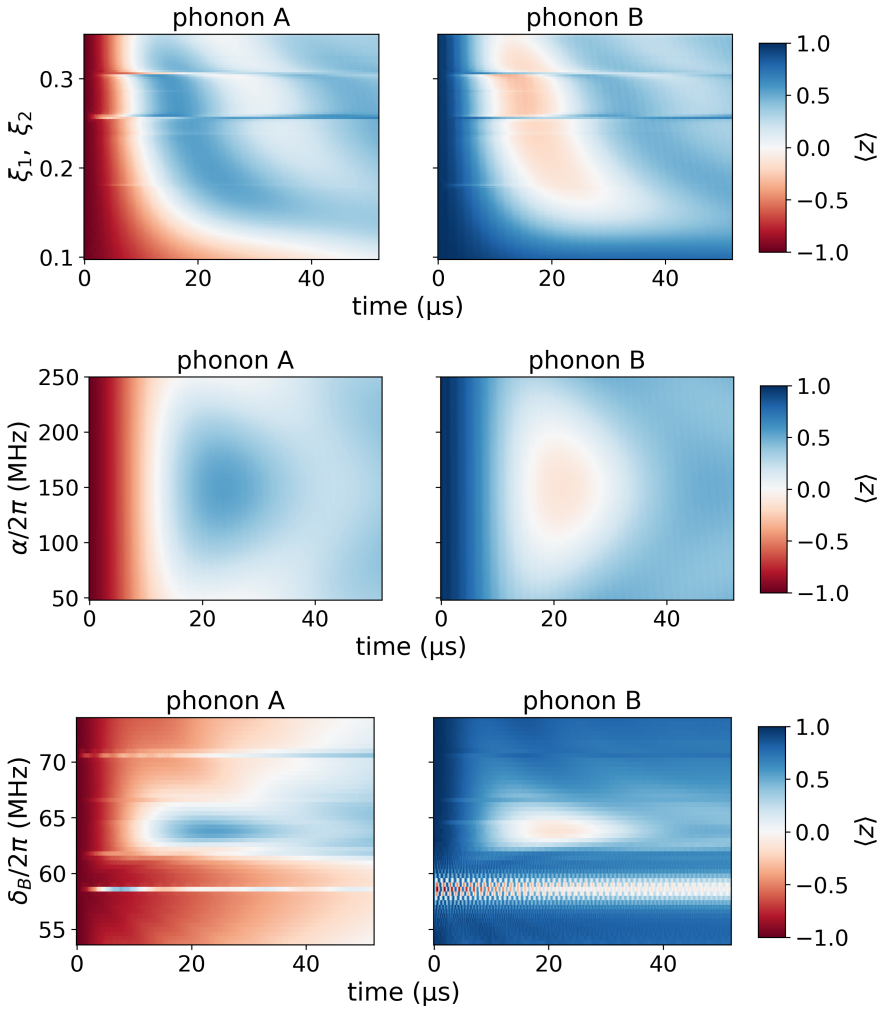

Figure 3.12.: Populations of phonon modes A, B and C against time and (top row) dimensionless drive strength ξ_1, (middle row) Kerr non-linearity α, and (bottom row) δ_B at the resonance condition of the SWAP gate ($\tilde{\delta}_1 = \tilde{\delta}_A - \tilde{\delta}_B + \tilde{\delta}_2$). There is an optimal range for the three parameters. The color scale and other parameters are the same as in Fig. 3.11.

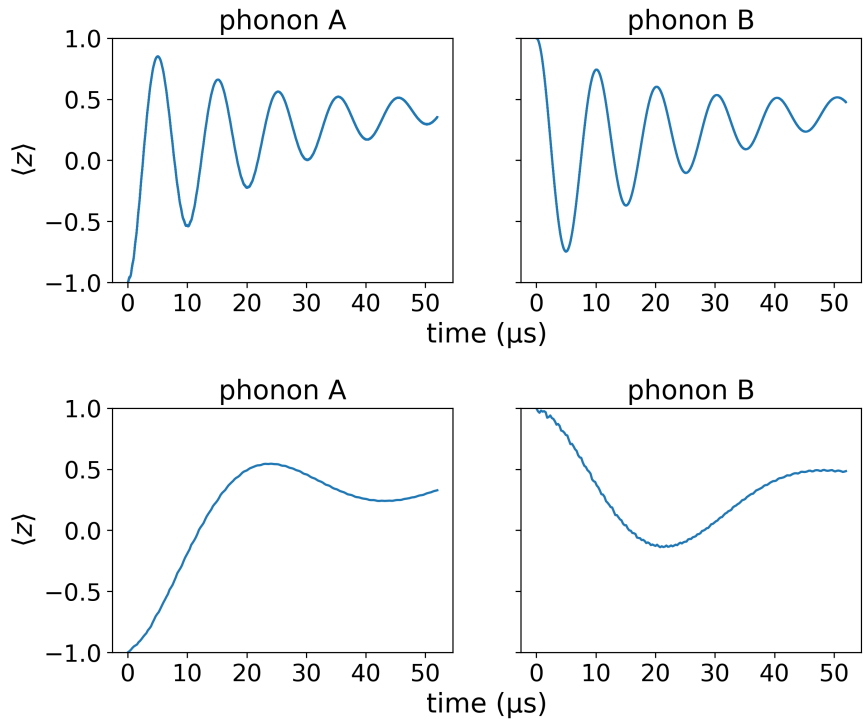

Figure 3.13.: Time evolution of the population of phonons A and B at the resonance condition of the SWAP gate ($\tilde{\delta}_1 = \tilde{\delta}_A - \tilde{\delta}_B + \tilde{\delta}_2$). The period of the oscillations considering the SWAP quartic term only (top row) is much shorter than when we consider the full cQAD Hamiltonian (bottom row). In both cases, the parameters are $\xi_1 = \xi_2 = 0.19$, $g/2\pi = 2.5$ MHz, $\alpha/2\pi = 150$ MHz, $\delta_A/2\pi = 44$ MHz, $\delta_B/2\pi = 64$ MHz, $\delta_C/2\pi = 26$ MHz, $\delta_2/2\pi = 79$ MHz.

3.4. Summary

In this chapter, we have investigated three operations that can be achieved in a cQAD system. Our predictions are based on a device in which a transmon qubit is piezoelectrically coupled to two high-overtone bulk acoustic resonators. Considering lifetimes of $T_1 = 7$ µs for the qubit and $T_1 = 100$ µs, $T_2 = 40$ µs for the phonons, previously reached in an $\hbar$BAR device [1], the phonon drive should be readily achievable. The CZ and SWAP gates are limited by the dephasing of the system, but, assuming that T_2 can be increased to 60 µs, both operations are promising experiments to perform in our system.

When studying the phonon drive, we first considered the interaction between a qubit and a single phonon to make preliminary estimates on reasonable drive strengths that can be applied to our system and on the size of the coherent state that can be achieved. Then, we identified parameters that allow for the implementation of the phonon drive considering the full system, and described discrepancies that arise with respect to the effects of the quartic interaction only. Likewise, the CZ and SWAP operations occur within a time frame different than that predicted by their quartic terms. Besides being limited by the dephasing of the phonons, both gates seem to require larger coupling strength than those currently achieved in an $\hbar$BAR device, although $g/2\pi$ of few MHz have been observed in similar systems [13, 26, 27].

Overall, the simulations suggest that we can drive the phonons into a coherent state and perform quantum operations in the cQAD system. While we can identify operations of interest and resonance conditions using individual quartic terms, the results presented in this chapter suggest that our system cannot be fully described with the fourth-order terms, but rather, we must take into account how these might be impacted by their lower-order counterparts and by coincidental resonances on the cQAD Hamiltonian.

Chapter 4

Conclusion

In this project, we have derived the expansion of the quartic terms of the cQAD Hamiltonian, identified the effects of interest starting from a pool of twenty-one terms and found their corresponding resonant conditions. Then, we used the quantum package QuTiP to simulate the time evolution of our system considering realistic qubit and phonon lifetimes. The simulations allowed us to identify potential parameters that can be used to experimentally effect the phonon drive, the CZ gate and the SWAP gate. Our results indicate that three parameters strongly influence the experiments: the spacing of the phonon modes, the coupling strength between the qubit and the phonon mode, and the strength of the drive tone.

Many challenges arise when observing the effect of the quartic terms in experimental conditions, i.e., when performing simulations using the full cQAD Hamiltonian. Competing effects seem to bring the timescale of the operations to the same order of magnitude as the relevant decay times of the phonons. For the investigated terms, the main limitation is predicted to be the dephasing of the phonons, T_2, which occurs in the same timescale as the CZ and SWAP gates when they are inserted in the full Hamiltonian of the system.

In the phonon drive case, we successfully identified the term responsible for the discrepancy in the frequency of the Rabi oscillations that arises when comparing the results of the cQAD Hamiltonian to those of the corresponding quartic term. Once the other sources of timing discrepancies are identified, and possibly mitigated, the next step would be to define and calculate the fidelity of the CZ and SWAP gates. This calculation could be achieved, for instance, by simulating the evolution for the six cardinal points on the Bloch sphere and comparing it to the ideal gate [28]. If our system can be engineered such that the quartic terms are dominant over the rest of the Hamiltonian—through the choice of mode spacing, for example—, we predict that high fidelities can be achieved, as in Ref. [2].

Throughout the course of this work, we have developed python scripts for different types of simulations, as well as predicted useful benchmarks to guide future experimental work. The developed capability of performing the summations corresponding to individual quartic terms greatly simplified previous methods and can be easily adapted to investigate the effects of any desired operation. Ultimately, we have identified and simulated operations of experimental relevance in a cQAD system, discussed their limitations and laid a computational background with promising directions to be further explored.

Appendix A

Simulation script

Sample simulation script on the example of the phonon drive

July 5, 2020

1 Initialization

[1]:
```
import numpy as np
from matplotlib import pyplot as plt
import matplotlib as mpl
from mpl_toolkits.mplot3d import Axes3D
from datetime import datetime
from mpl_toolkits.axes_grid1 import ImageGrid
import pprint
pp = pprint.PrettyPrinter(indent=4)
import qutip as qt
from itertools import combinations
import timeit
#load_ext memory_profiler
from memory_profiler import profile
from scipy import linalg as lg
from scipy.signal import argrelextrema
from scipy.signal import find_peaks
#layout
basefs=16
plt.rcParams['font.size'] = basefs
plt.rcParams['axes.titlesize'] = basefs+2
plt.rcParams['axes.labelsize'] = basefs+2
plt.rcParams['xtick.labelsize'] = basefs
plt.rcParams['ytick.labelsize'] = basefs
plt.rcParams['legend.fontsize']= basefs-2

def find(condition):
    res, = np.nonzero(np.ravel(condition))
    return res
```

Define Pauli matrices and states:

[2]:
```
sp = qt.sigmam()
sm = qt.sigmap()
sx = qt.sigmax()
sy = qt.sigmay()
sz = qt.sigmaz()
```

```
Id = qt.qeye(2)
vplus = 1/np.sqrt(2)*(qt.fock(2,0)+qt.fock(2,1))
vminus = 1/np.sqrt(2)*(qt.fock(2,0)-qt.fock(2,1))
vgr = qt.fock(2,0)
vex = qt.fock(2,1)
```

Define Pauli matrices for the Hilbert space composed of one qubit and three phonons:

[3]:
```
def spN(a,N=4):
    return qt.tensor([qt.qeye(2)]*a+[sp]+[qt.qeye(2)]*(N-a-1))
def smN(a,N=4):
    return qt.tensor([qt.qeye(2)]*a+[sm]+[qt.qeye(2)]*(N-a-1))
def sxN(a,N=4):
    return qt.tensor([qt.qeye(2)]*a+[sx]+[qt.qeye(2)]*(N-a-1))
def syN(a,N=4):
    return qt.tensor([qt.qeye(2)]*a+[sy]+[qt.qeye(2)]*(N-a-1))
def szN(a,N=4):
    return qt.tensor([qt.qeye(2)]*a+[sz]+[qt.qeye(2)]*(N-a-1))
```

[4]:
```
N = 4
# hilbert space is
# 0: qubit
# 1: phonon mode to be swapped from (A)
# 2: phonon mode to be swapped into (B)
# 3: some other phonon mode that we will need for the CZ gate (C)
# parameters (in MHz)
pi2 = np.pi * 2
```

Define plotting functions:

[5]:
```
def plot4modeEvolution(result,taxis, tickspace, savename, axis='xyz'):
    fig, ax = plt.subplots(2,2,figsize=(6,4),sharex=True, sharey=True)
    tn = 1
    titles = ['qubit', 'phonon A', 'phonon B', 'phonon C']
    for mind in range(N):
        x,y,z = result.expect[3*mind:3*(mind+1)]
        if 'x' in axis:
            ax[mind%2,mind//2].plot(taxis[::tn],x[::tn],label='x')
        if 'y' in axis:
            ax[mind%2,mind//2].plot(taxis[::tn],y[::tn],label='y')
        if 'z' in axis:
            ax[mind%2,mind//2].plot(taxis[::tn],z[::tn],label='z')

        ax[mind%2,mind//2].set_ylim([-1,1])
        ax[mind%2,mind//2].set_xticks(np.
↪arange(min(taxis),max(taxis),tickspace))
        ax[mind%2,mind//2].set_title(f'{titles[mind]}')
```

```
    # add a big axis, hide frame
    fig.add_subplot(111, frameon=False)
    # hide tick and tick label of the big axis
    plt.tick_params(labelcolor='none', top=False, bottom=False, left=False,␣
↪right=False)
    plt.xlabel(r'time ( s)')
    plt.ylabel(r'$\left\langle z \right\rangle$')
    plt.subplots_adjust(left=None, bottom=None, right=None, top=None,␣
↪wspace=None, hspace=0.4)
    plt.show()
    fig.savefig(savename,bbox_inches='tight',dpi=300)

def plot1modeEvolution(mind,result,taxis,tickspace,savename, axis='xyz'):
    fig, ax = plt.subplots(1, 1, figsize=(4, 3))
    tn = 1
    titles = ['qubit', 'phonon A', 'phonon B', 'phonon C']
    x,y,z = result.expect[3*mind:3*(mind+1)]
    if 'x' in axis:
        ax.plot(taxis[::tn],x[::tn],label='x')
    if 'y' in axis:
        ax.plot(taxis[::tn],y[::tn],label='y')
    if 'z' in axis:
        ax.plot(taxis[::tn],z[::tn],label='z')
    ax.set_ylim([-1,1])
    ax.set_xticks(np.arange(min(taxis),max(taxis),tickspace))
    ax.set_xlabel(r'time ( s)')
    ax.set_ylabel(r'$\left\langle z \right\rangle$')
    ax.set_title(f'{titles[mind]}')
    plt.tight_layout()
    plt.show()
    fig.savefig(savename,dpi=300)

def plot4modeBloch(result, tn=100, meth='l'):
    fig = plt.figure(figsize=(6,6))
    for mind in range(4):
        ax = fig.add_subplot(2,2,mind+1,projection='3d')␣
↪#Axes3D(fig,azim=-60,elev=30)
        b = qt.Bloch(axes=ax)
        b.clear()
        x,y,z = result.expect[3*mind:3*(mind+1)]
        b.add_points([x[::tn],y[::tn],z[::tn]], meth=meth)
        b.show()
```

Define operators:

[7]:
```
# bare operators
q = smN(0,N=N)
mA = smN(1,N=N)
mB = smN(2,N=N)
mC = smN(3,N=N)
qd = q.dag()
mAd = mA.dag()
mBd = mB.dag()
mCd = mC.dag()

# expectation values
e_ops = [sxN(0,N=N), syN(0,N=N), szN(0,N=N),
         sxN(1,N=N), syN(1,N=N), szN(1,N=N),
         sxN(2,N=N), syN(2,N=N), szN(2,N=N),
         sxN(3,N=N), syN(3,N=N), szN(3,N=N)]
```

Define collapse operators that take into account the lifetime of the qubit and of the phonons:

[8]:
```
#Coherence times in us
T1q = 7 #qubit
T1pn = 100 #phonon
T2pn = 40 #phonon

#construct collapse operators
c_ops = []
c_ops.append(np.sqrt(1/T1q) * smN(0,N=N))
c_ops.append(np.sqrt(1/T1pn) * smN(1,N=N))
c_ops.append(np.sqrt(1/T1pn) * smN(2,N=N))
c_ops.append(np.sqrt(1/T1pn) * smN(3,N=N))
c_ops.append(np.sqrt(1/T2pn) * szN(1,N=N))
c_ops.append(np.sqrt(1/T2pn) * szN(2,N=N))
c_ops.append(np.sqrt(1/T2pn) * szN(3,N=N))
```

Define exponential functions

[9]:
```
def exp_d_p(t,args):
    d = args['d']
    return np.exp(1j*d*t)
def exp_d_m(t,args):
    d = args['d']
    return np.exp(-1j*d*t)

#exp functions for single terms
def exp_4_p(dp,dq,dr,ds,t):
    return np.exp(1j*(dp+dq-dr-ds)*t)

def exp_4_m(dp,dq,dr,ds,t):
    return np.exp(-1j*(dp+dq-dr-ds)*t)
```

2 Simulations

2.1 Term XIX only

$-\frac{\alpha}{2}\sum_{hijl}\xi_h^*\xi_i^*\xi_j\lambda_k m_k e^{i(\delta_h+\delta_i-\delta_j-\delta_k)t}+\text{H.c.}$

for $\delta_1=\delta_A,\quad j=1$ (1 drive), $\quad k=A,\ B,\ C$ (3 phonons)

[10]:
```
wq = 6300
wA = wq + 74
wB = wA + 40
wC = wA - 20
w1 = wA
alpha = 150
g = 0.5
Ω1 = (w1-wq)*0.15
wq, wA, wB, wC, w1, alpha, g, Ω1 = list(np.array([wq, wA, wB, wC, w1, alpha, g,␣
↪Ω1])*pi2)
dA = wA - wq
dB = wB - wq
dC = wC - wq
d1 = w1 - wq

# dimensionless couplings
lambdaA = g/dA
lambdaB = g/dB
lambdaC = g/dC
lambdaAc = np.conj(lambdaA)
lambdaBc = np.conj(lambdaB)
lambdaCc = np.conj(lambdaC)

# dimensionless drive strengths
xi1 = Ω1/d1
xi1c = np.conj(xi1)

# effective time
pre_19 = (alpha/2)*4
g_19 = pre_19*(xi1c**2)*xi1*lambdaA
t_19 = np.pi/g_19

#Store parameters in lists, so that we can use loops to perform the summations
D_phonon = [dA,dB,dC]
D_drive = [d1]
Lambda = [lambdaA,lambdaB,lambdaC]
Lambda_c = [lambdaAc,lambdaBc,lambdaCc]
M = [mA,mB,mC]
Md = [mAd,mBd,mCd]
Xi = [xi1]
```

```
Xi_c = [xi1c]
```

Now we loop through the lists of variables defined in the previous cell in order to calculate the sums. The typical approach in QuTiP is to use the args variable, but this would require defining each term of the summation individually.

[11]:
```
t = np.linspace(0,t_19,1001)

H_19 = []
for h in range(1):
    for i in range (1):
        for j in range (1):
            for k in range (3):
                H_19.append([pre_19*Xi_c[h]*Xi_c[i]*Xi[j]*Lambda[k]*M[k],
                             ␣
 ↪exp_4_p(D_drive[h],D_drive[i],D_drive[j],D_phonon[k],t)])
                H_19.append([pre_19*Xi[h]*Xi[i]*Xi_c[j]*Lambda_c[k]*Md[k],
                             ␣
 ↪exp_4_m(D_drive[h],D_drive[i],D_drive[j],D_phonon[k],t)])

psi0 = qt.tensor([vgr,vgr,vgr,vgr])

H = [*H_19]
res_19 = qt.mesolve(H, psi0, t ,c_ops=c_ops,e_ops=e_ops,options=qt.
 ↪Options(nsteps=10001))
```

[12]:
```
tickspace=15
savenameA='200705_Term19_1D_A_1.png'
plot1modeEvolution(1,res_19, t,tickspace,savenameA,axis='z')
```

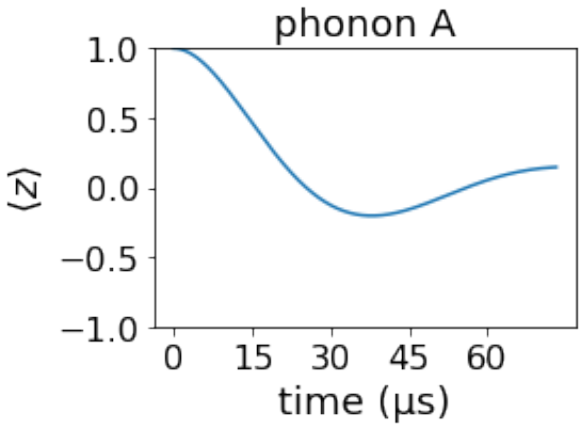

3 Full Hamiltonian with the resonance condition of term XIX

[13]:
```
wq = 6300
wA = wq + 74
wB = wA + 40
wC = wA - 20
w1 = wA
alpha = 150
g = 0.5
Ω1 = (w1-wq)*0.15
wq, wA, wB, wC, w1, alpha, g, Ω1 = list(np.array([wq, wA, wB, wC, w1, alpha, g,␣
↪Ω1])*pi2)
dA = wA - wq
dB = wB - wq
dC = wC - wq
d1 = w1 - wq

# dimensionless couplings
lambdaA = g/dA
lambdaB = g/dB
lambdaC = g/dC

# dimensionless drive strengths
xi1 = Ω1/d1
xi1c = np.conj(xi1)

# STARK SHIFTS
sA = -2*alpha*xi1**2*lambdaA**2
sB = -2*alpha*xi1**2*lambdaB**2
sC = -2*alpha*xi1**2*lambdaC**2
wAt = wA + sA
wBt = wB + sB
wCt = wC + sC

# dimensionless couplings stark
dAt = dA + sA
dBt = dB + sB
dCt = dC + sC
d1t = dAt

lambdaAt = g/dAt
lambdaAtc = np.conj(lambdaAt)
xi1t = Ω1/d1t
xi1tc = np.conj(xi1t)

# effective time
pre_19 = (alpha/2)*2*2
```

```
g_19 = pre_19*(xi1tc**2)*xi1t*lambdaAt
t_19 = np.pi/g_19
```

When considering the full Hamiltonian, we employ the args variable approach.

[14]:
```
H_anh = -alpha/2*qd*qd*q*q
H_pop_rwa = dA*mAd*mA + dB*mBd*mB + dC*mCd*mC

H_int = g*(mAd*q + mBd*q + mCd*q)
H_int = H_int + H_int.dag()

H0 = H_anh + H_int + H_pop_rwa
H_drive1 = [[Ω1*qd,exp_d_m], [(Ω1*qd).dag(),exp_d_p]]

psi0 = qt.tensor([vgr,vgr,vgr,vgr])

T = t_19
npoints = 401
t = np.linspace(0,T,npoints)

H = [H0, *H_drive1]
res_19 = qt.mesolve(H, psi0, t, args = {'d':d1t}, c_ops=c_ops,e_ops=e_ops,
                    options=qt.Options(nsteps=1001))
```

[15]:
```
tickspace=15
savenameA='200705_Res19_FullH_1D_A_1.png'
plot1modeEvolution(1,res_19, t,tickspace,savenameA,axis='z')
```

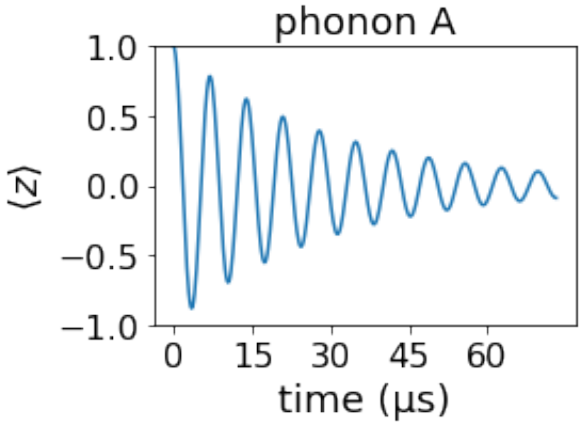

Bibliography

1. Chu, Y. *et al.* Creation and control of multi-phonon Fock states in a bulk acoustic-wave resonator. *Nature* **563,** 666–670. ISSN: 14764687. arXiv: 1804.07426. http://dx.doi.org/10.1038/s41586-018-0717-7 (2018).
2. Hann, C. T. *et al.* Hardware-Efficient Quantum Random Access Memory with Hybrid Quantum Acoustic Systems. *Physical Review Letters* **123,** 250501. ISSN: 10797114. https://doi.org/10.1103/PhysRevLett.123.250501 (2019).
3. Schreier, J. A. *et al.* Suppressing charge noise decoherence in superconducting charge qubits. *Physical Review B* **77** (2008).
4. Nigg, S. E. *et al.* Black-Box Superconducting Circuit Quantization. *Phys. Rev. Lett.* **108** (2012).
5. Chu, Y. *Quantum Acoustics and Optomechanics, Lecture 5* ETH Zürich, 2020.
6. Blais, A., Huang, R.-S., Wallraff, A., Girvin, S. M. & Schoelkopf, R. J. Cavity quantum electrodynamics for superconducting electrical circuits: An architecture for quantum computation. *Physical Review A* **69** (2004).
7. Gokhale, V. J. *et al.* Epitaxial bulk acoustic wave resonators as highly coherent multi-phonon sources for quantum acoustodynamics. *Nature Communications* **11.** https://doi.org/10.1038/s41467-020-15472-w (2020).
8. Safavi-Naeini, A. H., Thourhout, D. V., Baets, R. & Van Laer, R. Controlling phonons and photons at the wavelength scale: integrated photonics meets integrated phononics. *Optica* **6,** 213. https://doi.org/10.1364/OPTICA.6.000213 (2019).
9. Manenti, R. *et al.* Surface acoustic wave resonators in the quantum regime. *Physical Rview B* **93,** 041411(R) (2016).
10. Kharel, P. *et al.* Ultra-high-Q phononic resonators on-chip at cryogenic temperatures. *APL Photonics* **3,** 66101. https://doi.org/10.1063/1.5026798 (2018).
11. Maccabe, G. S. *et al.* Phononic bandgap nano-acoustic cavity with ultralong phonon lifetime. *arXiv:1901.04129v1.* arXiv: 1901.04129v1.
12. Lee, K. W. *et al.* Strain Coupling of a Mechanical Resonator to a Single Quantum Emitter in Diamond. *Phys. Rev. Applied* **6** (2016).
13. Manenti, R. *et al.* Circuit quantum acoustodynamics with surface acoustic waves. *Nature Communications* **8.** www.nature.com/naturecommunications (2017).
14. Moores, B. A., Sletten, L. R., Viennot, J. J. & Lehnert, K. W. Cavity Quantum Acoustic Device in the Multimode Strong Coupling Regime. *Physical Review Letters* **120** (2018).

15. Satzinger, K. J. *et al.* Quantum control of surface acoustic-wave phonons. *Nature* **563,** 661–665. https://doi.org/10.1038/s41586-018-0719-5 (2018).

16. Sletten, L. R., Moores, B. A., Viennot, J. J. & Lehnert, K. W. Resolving Phonon Fock States in a Multimode Cavity with a Double-Slit Qubit. *Physical Review X* **9** (2019).

17. O'connell, A. D. *et al.* Quantum ground state and single-phonon control of a mechanical resonator. *Nature* **464,** 697–703 (2010).

18. MacQuarrie, E. R. *et al.* Coherent control of a nitrogen-vacancy center spin ensemble with a diamond mechanical resonator. *Optica* **2,** 233–238. http://dx.doi.org/10.1364/OPTICA.2.000233 (2015).

19. Chu, Y. *et al.* Quantum acoustics with superconducting qubits. *Science* **358,** 199–202. ISSN: 10959203. arXiv: 1703.00342 (2017).

20. Kervinen, M., Rissanen, I. & Silllanpää, M. Interfacing planar superconducting qubits with high overtone bulk acoustic phonons. *Physical Review B* **97** (2018).

21. Chen, H. Y., Macquarrie, E. R. & Fuchs, G. D. Orbital State Manipulation of a Diamond Nitrogen-Vacancy Center Using a Mechanical Resonator. *Phys. Rev. Lett.* **120** (2018).

22. Leghtas, Z. *et al.* Confining the state of light to a quantum manifold by engineered two-photon loss. *Science* **347,** 853–857 (2015).

23. Gao, Y. Y. *et al.* Programmable Interference between Two Microwave Quantum Memories. *Physical Review X* **8,** 21073. ISSN: 21603308. arXiv: 1802.08510. https://doi.org/10.1103/PhysRevX.8.021073 (2018).

24. Zhang, Y. *et al.* Engineering bilinear mode coupling in circuit QED: Theory and experiment. *Physical Review A* **99,** 12314. ISSN: 24699934. arXiv: 1808.07960. https://doi.org/10.1103/PhysRevA.99.012314 (2019).

25. Nation, P. *et al. Solving Problems with Time-dependent Hamiltonians* 2020. http://qutip.org/docs/latest/guide/dynamics/dynamics-time.html.

26. Han, X., Zou, C.-L. & Tang, H. X. Multimode Strong Coupling in Superconducting Cavity Piezoelectromechanics. *Physical Review Letters* **117,** 123603 (2016).

27. Arrangoiz-Arriola, P. *et al.* Resolving the energy levels of a nanomechanical oscillator. *Nature* **571,** 537–540. https://doi.org/10.1038/s41586-019-1386-x (2019).

28. Grimm, A. *et al.* The Kerr-Cat Qubit: Stabilization, Readout, and Gates. *arXiv:1907.12131.* arXiv: 1907.12131v1.